Food Packaging and Shelf Life 33 (2022) 100919

Contents lists available at ScienceDirect

Food Packaging and Shelf Life

journal homepage: www.elsevier.com/locate/fpsl

Non-destructive online seal integrity inspection utilizing autoencoder-based electrical capacitance tomography for product packaging assurance

Jieming Pan [a], Zaifeng Yang [b], Stephanie Hui Kit Yap [a], Xiangyu Zhang [a], Zefeng Xu [a], Yida Li [a], Yuxuan Luo [a], Evgeny Zamburg [a], En-Xiao Liu [b], Chen-Khong Tham [a], Aaron Voon-Yew Thean [a,*]

[a] *Department of Electrical and Computer Engineering, National University of Singapore, 4 Engineering Drive 3, Singapore 117583, Singapore*
[b] *Institute of High Performance Computing (IHPC), A*STAR, Singapore, Singapore*

ARTICLE INFO

Keywords:
Electrical capacitance tomography
Autoencoder
Neural network
Image reconstruction
Nondestructive testing

ABSTRACT

Good quality packaging prevents contamination, secures preservation, and increases the ease of transportation in food and medical industries. One particular weakness of the package lies in the seal region where contents can be unintentionally incorporated, which disrupts the sealing process and compromises the structure and durability of the seal. To validate the seal quality effectively at high speed, a non-destructive high-resolution inspection approach combining enhanced sensors and reconstruction techniques is required. As the seal is flat and defects are minuscule, sensors have to be placed along the contour of the seal to achieve sufficient sensitivity. However, such conformal sensor placement poses new challenges to the ill-posed traditional tomography reconstruction. To overcome the limitation of sensing angle projections, imbalance in pixel representation and physical measurements, and asymmetric geometry of the sensed region, we propose a high-speed supervised autoencoder reconstruction approach. In this paper, our approach achieves high reconstruction image quality of irregular seal regions despite conformal sensor placement. While overcoming the limitations faced in traditional tomography, our model can be seamlessly integrated into the production line for real-time defect detection without affecting production speed and effectively minimizing manufacturing wastage and downtime.

1. Introduction

The food safety report published by the World Health Organization (WHO) in 2022 estimates that 600 million people, approximately 10% of the global population, fall ill after consuming contaminated food. Approximately 420,000 lives were taken every year due to diarrhea diseases induced by contaminated food and water (WHO, 2022). With a growing global population, the increase in demand for food has exacerbated the problems in food safety and poses new challenges in automated, clean, and high throughput packaging and preservation methods. Beyond the screening of poisonous substances in food products such as melamine in Sanlu milk powder (Jia, Huang, Luan, Rozelle, & Swinnen, 2012), poisonous starch found in Taiwan (Zuo, Wu, Gu, & Zhang, 2017), toxic fluorescent whitening agents as approved food additives in China, USA, and European Union (Poiger, Kari, & Giger, 1999; Wu et al., 2018), and heavy metal residues in chewable candies (Luiz et al., 2021), reliable packaging is the last line of defense to ensure consumers' safety (Graves, Smith, & Batchelor, 1998; Morita, Dobroiu, Otani, & Kawase, 2007; Reinas, Oliveira, Pereira, Mahajan, & Poças, 2016). However, the seal area, in particular, is prone to defects and contaminations introduced during high-throughput machine loading of flexible packaging of powder or liquid, thus compromising the structure and durability of the seal (Pan et al., 2020).

In high-throughput advanced manufacturing facilities, testing procedures are split into offline and online. Traditionally, offline testing relies on periodic random sampling, where manual labor inspection is adopted to recognize visually obvious defects. However, it is often too late when defects are identified since the high production rate could incur substantial product wastage. In contrast, online testing is more effective, reliable, and can perform accurate detection automatically and non-destructively at high speed. However, this is achieved at the expense of high complexity and high operating/development cost. Beyond the limitations of both online and offline testing procedures, determining weakened seals that do not lead to an obvious break is still a

---

* Corresponding author.
E-mail address: aaron.thean@nus.edu.sg (A.V.-Y. Thean).

https://doi.org/10.1016/j.fpsl.2022.100919
Received 13 January 2022; Received in revised form 22 June 2022; Accepted 28 July 2022

Table 1
Comparison of existing test methods in ensuring quality assurance of product packaging.

Test method							
Criteria	**Ultrasonics**	**X-ray**	**Eddy current**	**Magnetic particle**	**Vacuum / Burst**	**Liquid penetrant**	**Our Work**
Time of results	Immediate	Delayed	Immediate	Short delay	Short delay	Short delay	Immediate
Effect of geometry	Important	Important	Important	Not too important	Not too important	Not too important	Not too important
Type of defect	Most	Most	External	External	Breaking Leaking	Breaking Leaking	Most
Relative sensitivity	Minimum 10 μm diameter channel defect	Minimum length 1.5 mm metalic fragments	Minimum length 0.8 mm depth 0.125–1.75 on the surface of metalic packaging	Minimum length 7 mm on the surface of metalic packaging	Only when leaking or breaking	Only when leaking or breaking	120 μm micro-particles within the package
Portability of equipment	High	Low	High to medium	High to medium	High to medium	High	High to medium
Dependent on material composition	Difficult to use on thin and relatively rough materials	Changes in thickness, density, and/or elemental composition	Material must be electrically conductive or magnetic	Magnetic only	Little dependency	Little dependency	Little dependency
Ability to automate	Easy to integrate onto the production line	Able to integrate on production line with additional setup and delay	Easy to integrate onto the production line	Easy to integrate onto the production line	Able to integrate on production line with additional setup and delay	Able to integrate on production line with additional setup and delay	Easy to integrate onto the production line
Capabilities	Thickness gaging: some composition testing	Thickness gaging	Thickness gaging; grade sorting	Defects only	Breach, leakage, defects	Breach, leakage, defects	Thickness, gaps, breach, defects, contaminant, grade sorting

significant challenge. Existing test methods such as vacuum, pressure decay, differential force measurement, bubble test, and helium leak detection test, suffer from poor sensitivity and require offline destructive screening at low throughput (Kirsch, 2007; Sand, 2019). Non-invasive methods like acoustic, ultrasound, and X-ray imaging techniques are costly, slow, and package materials dependent (Ayhan, Zhang, Farahbakhsh, & Kneller, 2001; Schoeman, Williams, du Plessis, & Manley, 2016). Table 1 lists the advantages and disadvantages of different seal detection methods (Charles, 2013; Raum, Ozguler, Morris, & O'Brien, 1998; Sand, 2019; Whittaker, 1972). To ensure the quality of every package leaving the manufacturing plant, a non-destructive and fast seal integrity detection method needs to be integrated seamlessly onto the production line.

The capacitive sensor is a passive device (Li, Alian et al., 2019; Xiong, Li, Thean, & Heng, 2019) that is capable of proximity sensing (Pan et al., 2021; Ye et al., 2020), displacement sensing (Li & Luo, 2019; Luo, Li, Thean, & Heng, 2020; Ye et al., 2020), material sensing (Hamanaka, Segundo, & Silva, 2017; Yap et al., 2022; Zhang, Zeng, Teng, & Zhang, 2017), and humidity sensing (Xu, Weber, & Kasper, 2000). Apart from the fast sensing speed, the capacitive sensor is non-destructive and scalable, allowing it to be placed closely around the target to maximize sensor sensitivity. Together with the advancement in analog sensing circuits, capacitive sensors can be seamlessly integrated into the production line for real-time inspection. Additionally, reconstruction algorithms such as Electrical Capacitance Tomography (ECT) (Marashdeh, Fan, Du, & Warsito, 2008; Smith et al., 1998; Tiefenbacher, 2018; Yang, Lu, & Zhou, 2018) can be adapted to further increase the sensor resolution for more accurate defect detection.

As the seal is flat and defects are minuscule, capacitive sensors have to be placed along the contour of the seal to maximize sensor sensitivity. The conformal placement, however, introduces new challenges to the ill-posed traditional tomography approaches that are limited by the sensing angle projections, the asymmetric number of pixels and measurements, and the geometry of the sensed region to produce a high-resolution reconstructions. Here, we designed an efficient machine learning model based on a supervised autoencoder to ensure high-quality reconstruction even with conformal sensor placement. Each successfully reconstructed relative permittivity distribution image contains an accurate representation of the defects within the seal both visually and quantitatively for extensive spatial analysis and it can be produced in just 1.1 ms on a regular computer. In addition to overcoming the limitations faced in traditional tomography approaches, our model can be seamlessly integrated into the production line for real-time defect detection without affecting production speed and minimizing wastage and downtime.

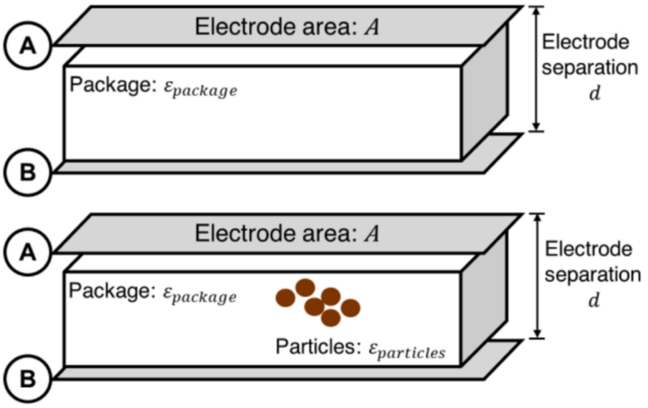

Fig. 1. Illustrations of a parallel plate electrode with electrodes A and B covering an area of A with a separation of d.

2. Materials and methods

2.1. Non-destructive capacitive sensing

The capacitive sensing mechanism is based on measuring the changes in the capacitance due to the surrounding dielectric perturbation (Gallagher & Moussa, 2014; Li et al., 2019; Pillai, 1970). In the simplest parallel plate capacitive sensing setup shown in Fig. 1, the capacitance between two electrodes with a flat electrode area A and a perpendicular separation of d can be expressed in its closed form as:

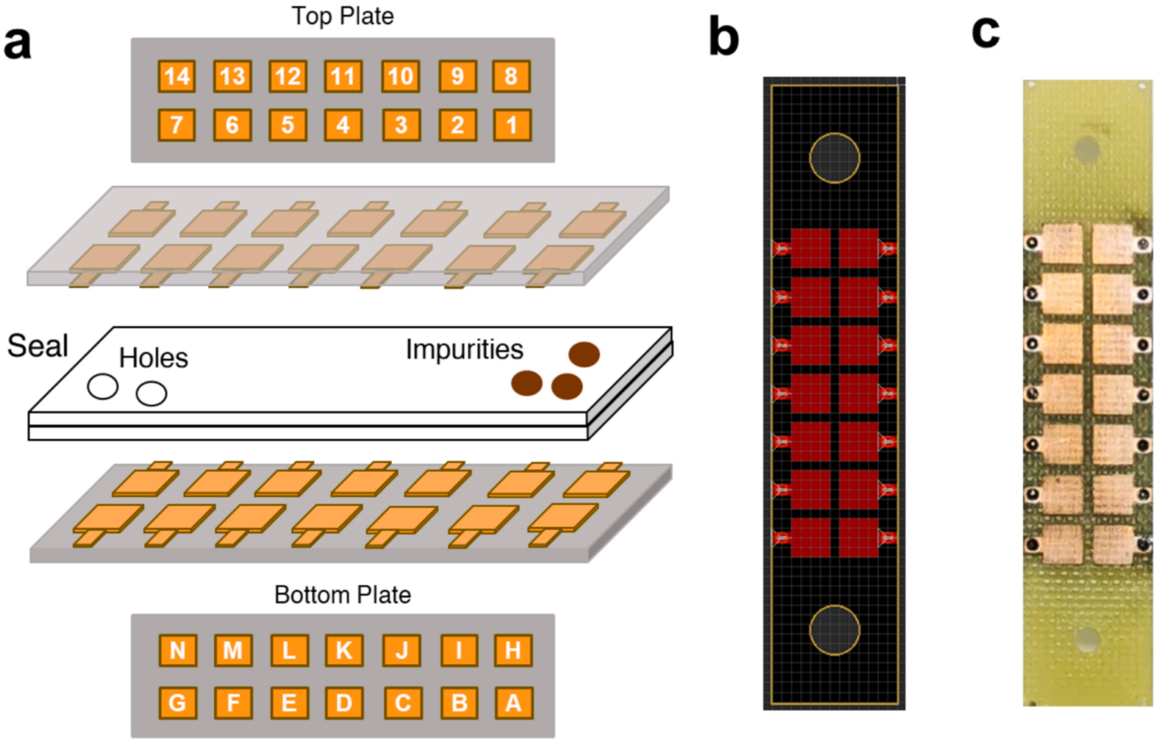

Fig. 2. Illustrations of (a) 14 electrodes sensor array model with electrode labeling, and (b) the schematic of sensor array electrodes. (c) Image of the fabricated capacitive sensor array on the Printed Circuit Board (PCB).

$$C_{parallel} = \varepsilon_r \varepsilon_0 \frac{A}{d} + C_{fringe} \tag{1}$$

where $\boldsymbol{\varepsilon_r}$ is the relative permittivity of the material between the electrode separation and $\boldsymbol{\varepsilon_0}$ is the permittivity of free space, assuming the effect of the fringe field is negligible (Dimitrov et al., 2020). Eq. (1) suggests that the change in the materials between the sensing electrodes has a direct impact on the measured capacitance if the area of each electrode and the distance between opposing electrodes are kept constant. However, the detection sensitivity in this setup is also influenced by the sensing area and the distance separating the electrodes. For instance, as the electrode area increases and the electrode separation decreases, the measured capacitance increases drastically which reduces the significance of capacitance change due to the effect of dielectric perturbation. This consequence becomes more severe for materials with a low relative permittivity. Furthermore, as the measured capacitance is contributed by the sum of the electric field of the sensing area, it is not feasible to identify the exact location of the introduced particles. To overcome the obvious tradeoff between the effective sensing area and sensitivity, an array of electrodes is used simultaneously to expand the sensing area and increase the spatial information captured without compromising sensitivity (Pan et al., 2020).

2.2. Sensor design and verification

While the parallel plate capacitive sensors can directly detect anomalies and particles in the packages non-destructively, the sensitivity and location capability are still limited. To overcome this limitation, an array of 14 smaller electrodes is designed to increase the sensing resolution and provide valuable position information of the particles as shown in Fig. 3. The full-wave simulation of the 14 electrode pairs sensor array is created using COMSOL Multiphysics software and the detailed parameters used are shown in Supplementary S1 and Supplementary S2 respectively. The sensing capability is first evaluated with COMSOL simulation followed by experimental verification. The replica of the simulated sensor array is fabricated using the Printed Circuit Board (PCB) prototyping machine LPKF ProtoMat S63 as shown in Fig. 2**b & 2c**. The electrical properties are measured using the Keysight E4980AL LCR meter at 100 kHz to avoid the 50 Hz powerline noise. For the sensor array, the top electrodes are labeled from 1 to 14 and the bottom electrodes are labeled from A to N as shown in Fig. 2**a**, forming groups of opposing electrodes in pairs 1A, 2B, …, 14N, respectively. The defect particles are colored in brown, and their exact locations are shown in Fig. 3**a**.

The simulation results presented as the heat map in Fig. 3**b** show a significantly higher capacitance value when particles are located between the testing electrodes. Evidently, the perpendicular electrode pairs 1A, 4D, 5E, 9I, and 11K have a much higher capacitance value as compared to other electrode pairs that are away from the particles. Apart from the significant increase in capacitance in 4D, 9I, and 11K, the neighboring and diagonal electrode pairs 2A, 1B, 6E, and 5F also indicated a substantial increase since the particles are located between the adjacent electrodes. Given the capacitance of all combinations of electrode pairs, the exact location and even the material of the particle can then be calculated directly.

Experimentally, both the profile of the packaging and the location of particles can be effectively identified through corresponding capacitance measurement as shown in Fig. 3**c**. For instance, the fold in the middle of the seal located around positions 3C and 4D causes a 0.587e^{-13} F increase in capacitance as compared to the average increase of 0.243e^{-13} F at the remaining seal area. The capacitance increase experienced at the fold is almost double (blue boxes) that at the remaining seal area, which interestingly coincides with the 2:1 ratio between the number of plastic layers at each location shown in Fig. 3**c & 3e**. The location of the particles can be verified by comparing the capacitance between electrode pairs and the image of the plastic package with 20 mg of particles incorporated as shown in Fig. 3**c & 3d**. The smallest capacitance changes of 8.0e^{-15} F, 6.8e^{-15} F, and 9.6e^{-15} F are captured at electrode positions 1A, 8H, and 10J respectively (green boxes). The largest capacitance changes of 4.18e^{-14} F, 3.64e^{-14} F, and 4.87e^{-14} F are captured at electrode positions 7G, 9I, and 14N respectively (red boxes). The image of the

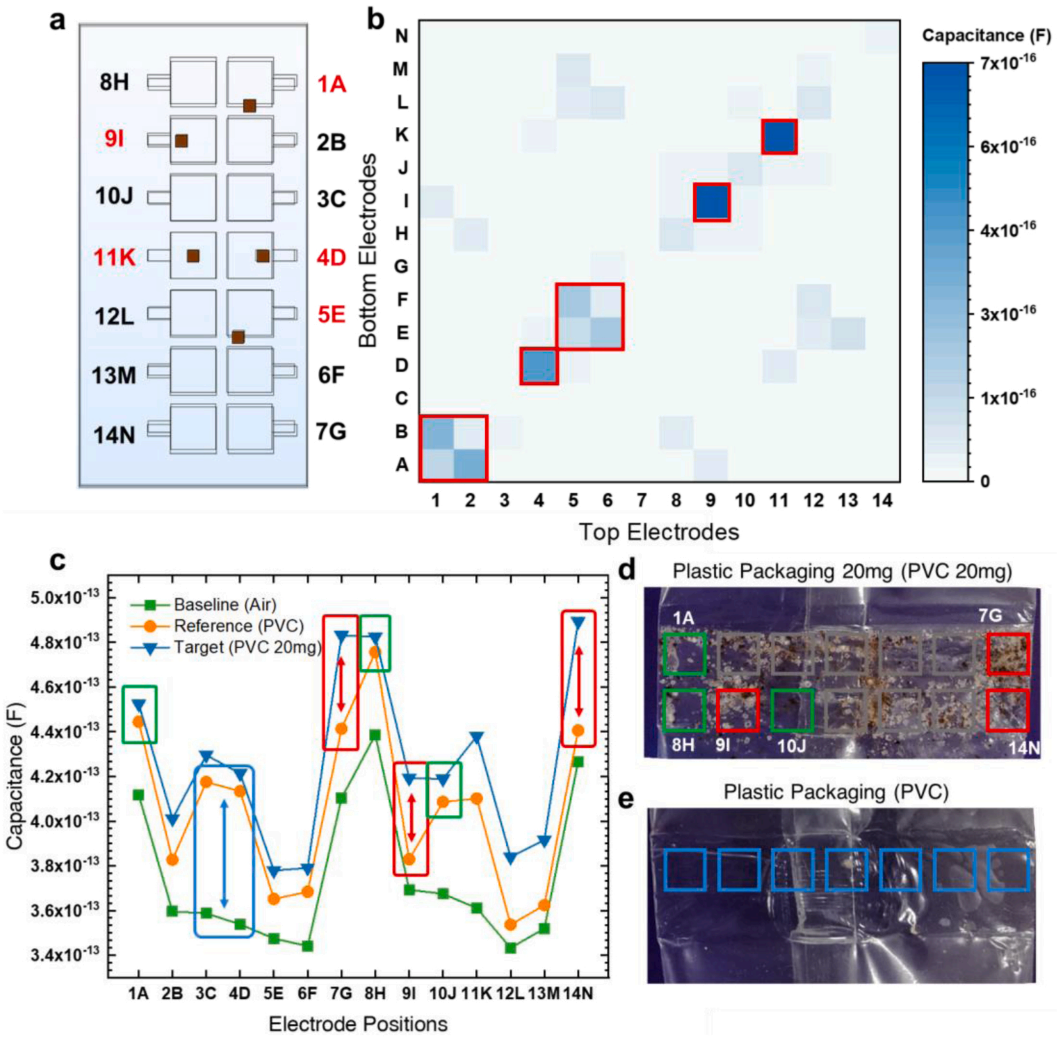

Fig. 3. (a) COMSOL simulation of 14 electrode pairs and the respective particle location. (b) Heat map of all combinations of pairwise capacitance difference measurement with defect particles. (c) Cross-validation of change in capacitance measurement across all electrode pairs with, (d) image of the package with incorporated particles distribution, and (e) the profile of a PVC package with respect to electrode positions.

transparent package provides visual verification of the relationship between measured capacitance and the incorporated particles at various locations. However, due to gaps between the neighboring electrodes, the relative permittivity distribution in the sensed region is discontinuous, and pinpointing the exact location of the particle remains challenging. Reconstruction techniques are hence required to achieve a continuous relative permittivity distribution map, which is crucial in determining the quality of the package as well as providing valuable insights into reasons for such defects and thus improving maintenance and ensuring product quality and yield.

2.3. *Electrical capacitance tomography with linear back projection*

Electrical Capacitance Tomography (ECT), first proposed in 1980, is the most common and popular technique to reconstruct the relative permittivity distribution from a set of capacitance measurements (Buzug, 2011; Herman, 2009). This technique requires an array of electrodes placed around the imaging domain to measure the capacitance change and a reconstruction algorithm to compute the relative permittivity distribution of the internal structure. Some examples of classical reconstruction algorithms include Linear Back Projection (LBP) algorithm (Sun, Yue, Cui, & Wang, 2015), Algebraic Reconstruction Technology (ART) (Andersen & Kak, 1984; Raparia, Alessi, & Kponou, 1997), Singular Value Decomposition (SVD) (Van Loan, 1976; Wall, Rechtsteiner, & Rocha, 2003), and Extreme Learning Machine (ELM) (Huang, Zhu, & Siew, 2006). These algorithms usually have a fast reconstruction speed but poor image resolution. Meanwhile, other algorithms such as Landweber iterative method (Hanke, Neubauer, & Scherzer, 1995) and the Tikhonov regularization algorithm (Calvetti & Reichel, 2003; Golub, Hansen, & O'Leary, 1999) offer better imaging accuracy by increasing the stability and controlling the noise in the reconstruction. With the recent advancements in artificial intelligence, neural network approaches have also been incorporated and achieved significant success (Wang, Liu, Chen, Yang, & Wang, 2020; Zheng & Peng, 2018).

The basic principle of these approaches is to approximate the nonlinear relationship between the measured capacitance and the permittivity distribution. Derived from Maxwell's first equation, the relationship between the relative permittivity $\varepsilon(x, y)$, the potential distribution of the electrical field $\phi(x, y)$, and the charge density $\rho(x, y)$ in a two-dimensional space follows

$$\nabla \bullet \varepsilon(x, y)\nabla\phi(x, y) = -\rho(x, y) \tag{2}$$

In the forward problem, the capacitance value $C_{n,k}$ of the electrode pair n and k are obtained by integrating (2):

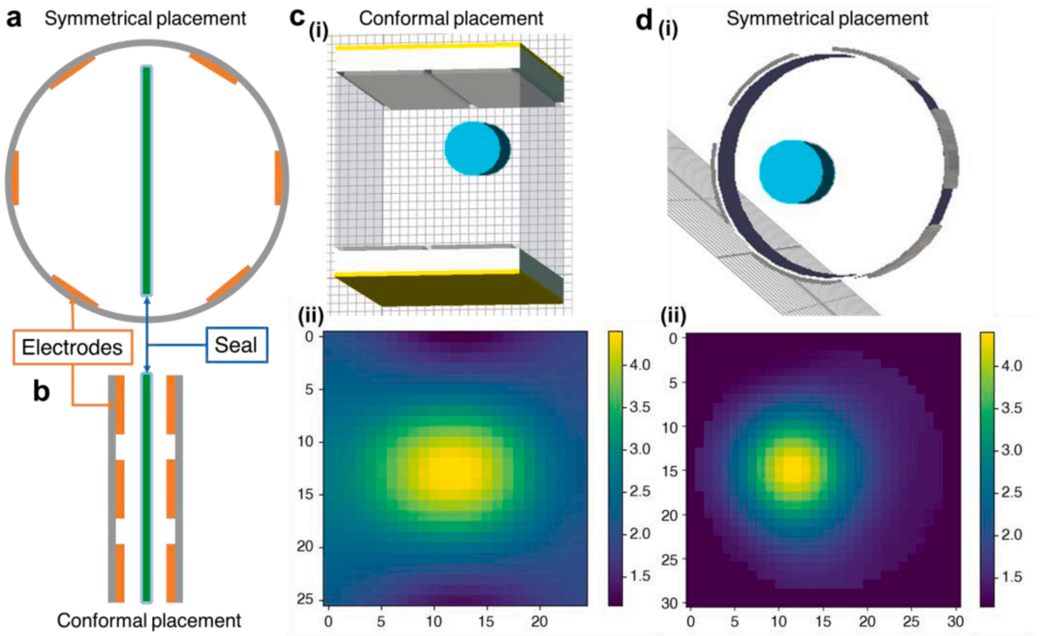

Fig. 4. (a) Cross-sectional view of the symmetrical placement of electrodes. (b) Cross-sectional view of the conformal placement of electrodes. (c)(i) Simulation of conformal placement with a single particle and the (c)(ii) LBP reconstructed image. (d)(i) Simulation of symmetrical placement with a single particle and the (d)(ii) LBP reconstructed image.

$$C_{n,k} = -\frac{1}{V}\iint_{\Gamma} \varepsilon(x,y)\nabla\phi(x,y)d\Gamma \tag{3}$$

where Γ represents the enclosed imaging area and V is the potential difference between the two electrodes. In a common ECT setup, the electrode pairs are placed uniformly around a circular imaging area to ensure equal sensing distance. The linearization technique based on the superposition theorem subdivides the imaging area into pixels and the solution to the forward problem becomes the sum of responses due to change of permittivity at individual pixels. With linearization, the relation between the capacitance matrix of electrode pairs and relative permittivity distribution in the imaging area can be approximated by the matrix expression:

$$C = SG \tag{4}$$

where C is the capacitance matrix of various electrode pairs, G is the image vector of Γ, S is approximated sensitivity matrix similar to the first-order series expansion of the electric field in Γ.

$$G = S^T C \tag{5}$$

To reconstruct the image vector G from the measured capacitance matrix C, we can solve the inverse of the sensitivities matrix S which is represented as the transpose S^T as shown in Eq. (5). However, the total pixels of the reconstructed image is often much larger than the number of measured capacitance values causing the problem to be ill-posed. Through back projection, the measured capacitance data can be summed into the image vector. However, the final output suffers from a smoothing effect, giving a rough estimation of the relative permittivity distribution in the imaging domain.

$$C' = SG \tag{6}$$

To solve this issue, iterative methods such as Landweber are commonly used to iteratively improve the reconstructed image stability and control image noise by minimizing the error between the measured C to the estimated C' as shown in Eq. (6).

While existing approaches have shown promising results in multiphase flow, medical imaging (Bach et al., 2012), non-destructive testing (De Schryver et al., 2016; Schoeman et al., 2016), and security (Shikhaliev, 2018) domains, such reconstruction techniques are limited by the need for the symmetrical placement of electrodes. In seal quality assurance, the seal area in packages is often small, irregular, and flat, and the relative permittivity of defects is low. Instead of the symmetrical placement of electrodes in a circle, conformal placement along the contour of the seal is necessary to capture the minute capacitance differences between a good and defective seal as shown in Fig. 4**a & 4b**. However, the new placement introduces additional non-linearity in the system which adversely affects the reconstruction quality of projection-based algorithms. This is illustrated in Fig. 4**d(ii) & 4c(ii)**, where the quality of reconstructed relative permittivity distribution images based on different electrode placements is compared. Using the same LBP algorithm, the reconstructed image based on symmetrically placed electrodes reveals the clear location and size of the introduced defect (blue cylinder) but fails to do so with the conformal placement. This is because the non-uniform distance between different electrode pairs becomes an additional component contributing to measured capacitance which significantly increases the system complexity for reconstruction. Supplementary S3 presents the sensitivity matrix between the electrode pairs in a conformal placement, which highlights significant non-linearity due to non-uniform separation between electrodes. In order to benefit from the enhanced sensor sensitivity conformal sensor placement offers, the aforementioned constraint can be minimized by implementing a new data-driven approach to reconstruct the relative permittivity distribution of the sensed region successfully.

2.4. Autoencoder neural network

Along with the success of its predecessors, the Generative Adversarial Networks (GAN) (Goodfellow et al., 2014) introduced in 2014 has achieved excellent performance in estimation tasks. Briefly, Artificial Neural Network (ANN) mimics the human brain and learns to model a specific task for predictions and classifications, Convolutional Neural Network (CNN) uses filters capable of extracting the spatial information in the data and is exceptional with image data, and Recurrent Neural Network (RNN) adopts the concept of states which acts as a form of

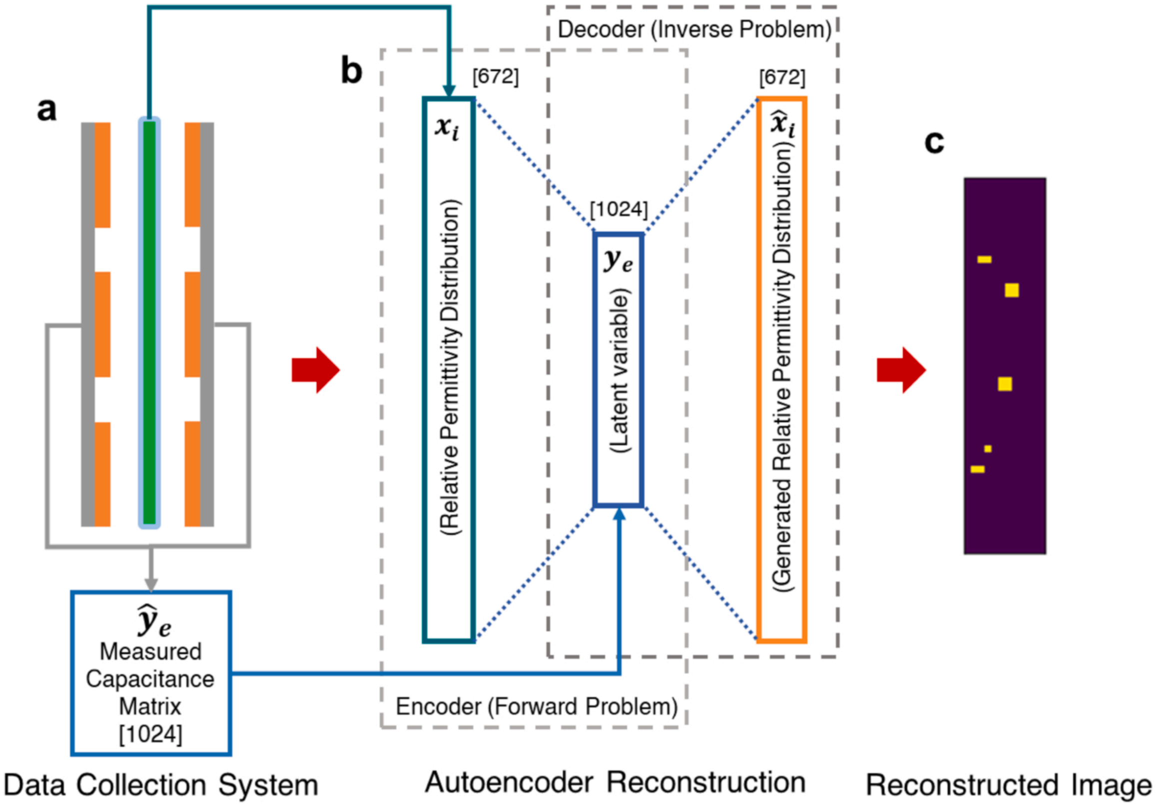

Fig. 5. System flow of the autoencoder neural network reconstruction approach from (a) the conformal placement of electrode for capacitance measurement to (b) providing relative permittivity distribution and the measured capacitance matrix as the inputs and eventually (c) reconstruction output from the decoder.

memory designed to understand temporal information in sequential datasets (Alzubaidi et al., 2021). GAN, on the other hand, introduces competition between the generative model and the discriminative model through the adversarial process to improve the models' accuracy simultaneously. Using a compression and reconstruction process, GANs have achieved significant success in super-resolution (Gupta et al., 2021) image processing which makes the supervised autoencoder neural network an ideal candidate for image reconstruction. Similar to tomography, the supervised autoencoder neural network learns the relationship between the sensed signals and the ground truth of the scanned region to create an accurate replica of the relative permittivity distribution.

Based on physics theory, traditional tomography approaches use inverse models and iterative optimization to derive the relative permittivity distribution of the imaging domain. However, these approaches are ill-posed and limited by the sensing angle projections, the asymmetric number of pixels and physical measurements, and the geometry of the sensed region. Neural networks, on the other hand, learn patterns and solutions from a set of training data and generalize it to extended unseen test data. Such approaches have been widely adopted in Computed Tomography (CT) of medical imaging (Arridge, 1999) and ECT of the multi-phase flow process (Yao & Takei, 2017). The proposed autoencoder neural network reconstruction approach composed of the encoder and decoder, as shown in Fig. 5, is a supervised learning model that functions as a general estimator to map complex relationships between the measured capacitance to the relative permittivity distribution of the imaging domain. The input data is first compressed onto a latent space by the encoder and decompressed by the decoder back into the reconstructed form of the input. The objective of the autoencoder is to learn a function that reconstructs accurate input data from a latent representation. In a single hidden layer autoencoder, the latent variable y_e is the function of the input x_i and the reconstructed output $\widehat{x}_i$ is a function of the latent variable y_e as shown in Eq. (7) & (8).

$$y_e = f_e(W_e x_i + b_e) \tag{7}$$

$$\widehat{x}_i = f_d(W_d y_e + b_d) \tag{8}$$

where, f_e is the non-linear activation function applied to the input layer, W_e and W_d are the encoder and decoder weights respectively, b_e and b_d are the encoder and decoder biases respectively. Physically, the relative permittivity distribution x_i directly influence the capacitance between different pairs of electrodes. By adding an addition loss function between the capacitance matrix and latent variable y_e, the autoencoder can learn this relationship in a supervised manner, as shown in Fig. 5**b**. In our model, Mean Square Error (MSE) is used as the loss function for learning.

$$L_{total} = L_x\alpha_x + L_y\alpha_y \tag{9}$$

$$L_x = \frac{1}{mn}\sum_{i=0}^{m-1}\sum_{j=0}^{n-1}\left[X(i,j) - \widehat{X}(i,j)\right]^2 \tag{10}$$

$$L_y = \frac{1}{mn}\sum_{i=0}^{m-1}\sum_{j=0}^{n-1}\left[Y(i,j) - \widehat{Y}(i,j)\right]^2 \tag{11}$$

where L_{total} is the total loss function used in the autoencoder training process, L_x is MSE loss between the input image X and the decoded output image $\widehat{X}$, L_y is the MSE loss between the input capacitance matrix $\widehat{Y}$ and the latent space matrix Y, α_x is the weight for L_x, α_y is the weight for L_y. During training, the autoencoder will adjust the weights W_e and W_d at each layer to minimize the losses highlighted in Eqs. (9), (10), and (11).

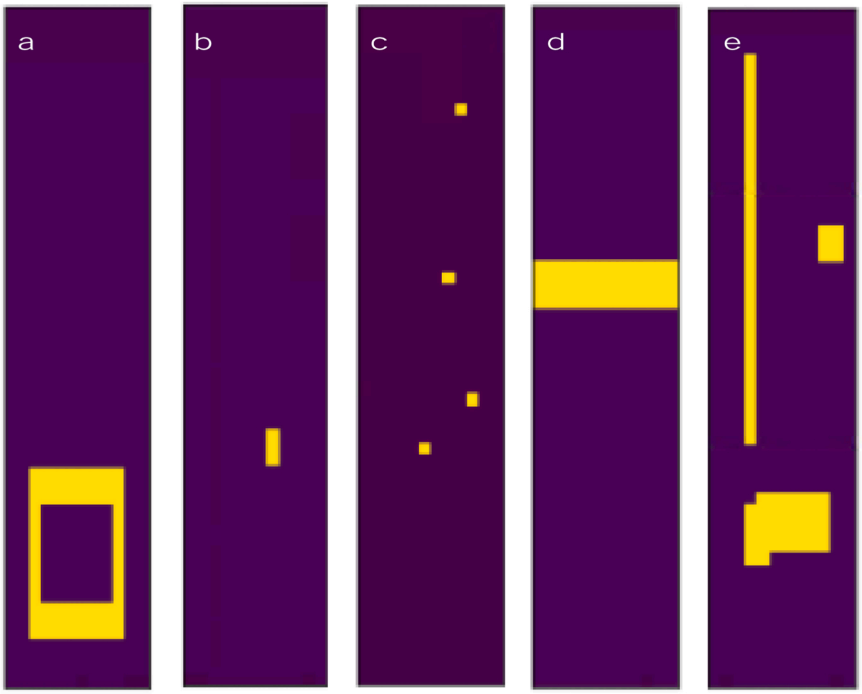

Fig. 6. The five categories of defect particles distribution: (a) round, (b) spot, (c) scatter, (d) through, and (e) mix.

2.5. COMSOL simulation and experiment verification

To obtain a training dataset that captures the nonlinear relationship between the measured capacitance value and the internal relative permittivity distribution, a three-dimensional (3D) 16 electrode pairs conformal ECT sensor model is developed using the finite element analysis simulation in COMSOL Multiphysics. The two additional electrodes on each plate ensure better coverage of the entire package. Using electrostatic physics in the AC/DC module, five types of defects are introduced at varying locations within the sensing region as shown in Supplementary S4. They are categorized as round, spot, scatter, through, and mix shown in Fig. 6. In each simulation, we extract the relative permittivity distribution of the seal center X and the capacitance matrix $\widehat{Y}$ of all combinations of electrode pairs (i,j).

A total of 313 defect distribution samples and their respective capacitance matrices are generated for autoencoder network training. The dataset is split into 12 unseen test samples, consisting of two or three randomly selected defect distributions from each category, and a training set of 301 samples. Each data sample pair contains a normalized permittivity distribution vector, x_i, of 12 by 56 pixels with a total of 672 elements. As such, each pixel covers an area of 0.536 mm^2 within the 10 mm by 36 mm seal region without significantly increasing the computational cost of the autoencoder model shown in Supplementary S5. The corresponding normalized capacitance vector of the 16 electrode pairs ECT sensor array, y_e, consists of 1024 elements and is obtained through a thorough scan between all combinations of the 32 electrodes. The materials of the sensor, seal package, and defect particles are set to be copper with relative permittivity of 6.0, PVC with relative permittivity of 3.2, and food particles with relative permittivity of 80 respectively.

3. Results and discussion

3.1. Reconstructed image evaluation matrix

To evaluate the reconstruction quality, the mean square error and correlation coefficient between actual permittivity distribution and reconstructed permittivity distribution are taken as the criteria of autoencoder performance. They are commonly used in ECT image reconstruction to evaluate reconstruction quality quantitatively (Zheng & Peng, 2018). The Correlation Coefficient (COR) (Yang & Peng, 2002) indicates the similarity between the reconstructed permittivity distribution and the original permittivity distribution, which is defined as Eq. (12) and denoted by *cor*,

Table 2
The 10-fold cross-validation correlation coefficient score and mean square error.

Correlation Coefficient Score of 10 Fold Cross-validation					Mean Square Error of 10 Fold Cross-validation				
Fold Number	Average	Std	Min	Max	Fold Number	Average	Std	Min	Max
1	0.6852	0.1875	0.2707	0.9606	1	0.0195	0.0172	0.0027	0.075
2	0.6435	0.2035	0.1287	0.8694	2	0.0408	0.0455	0.0087	0.1924
3	0.6782	0.1859	0.3051	0.8913	3	0.0288	0.0349	0.0036	0.1711
4	0.7162	0.1329	0.3503	0.9549	4	0.0345	0.0413	0.007	0.1735
5	0.6875	0.1704	0.3051	0.8779	5	0.023	0.0188	0.0041	0.0744
6	0.6419	0.2106	0.2663	0.9057	6	0.0346	0.0497	0.0038	0.194
7	0.719	0.1517	0.3341	0.9116	7	0.0417	0.0471	0.0097	0.1762
8	0.6183	0.1982	0.2406	0.8481	8	0.042	0.0543	0.0053	0.2235
9	0.7098	0.1385	0.3224	0.8396	9	0.0235	0.0198	0.0035	0.0982
10	0.6036	0.1985	0.2618	0.8696	10	0.0306	0.0336	0.0042	0.1689
Average	0.6703				Average	0.0319			

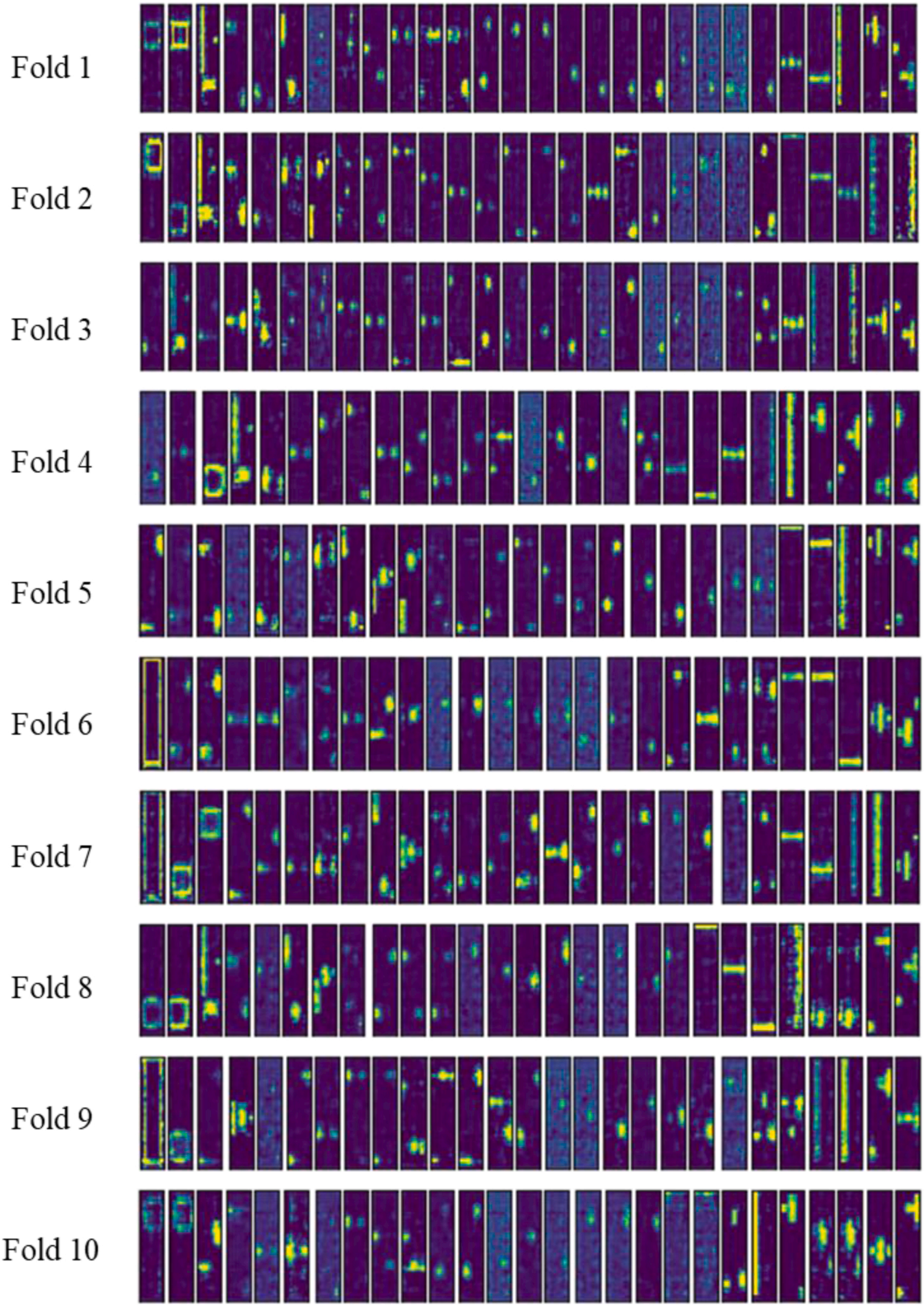

Fig. 7. The reconstructed images of particles distribution in each fold of the 10-fold cross-validation process.

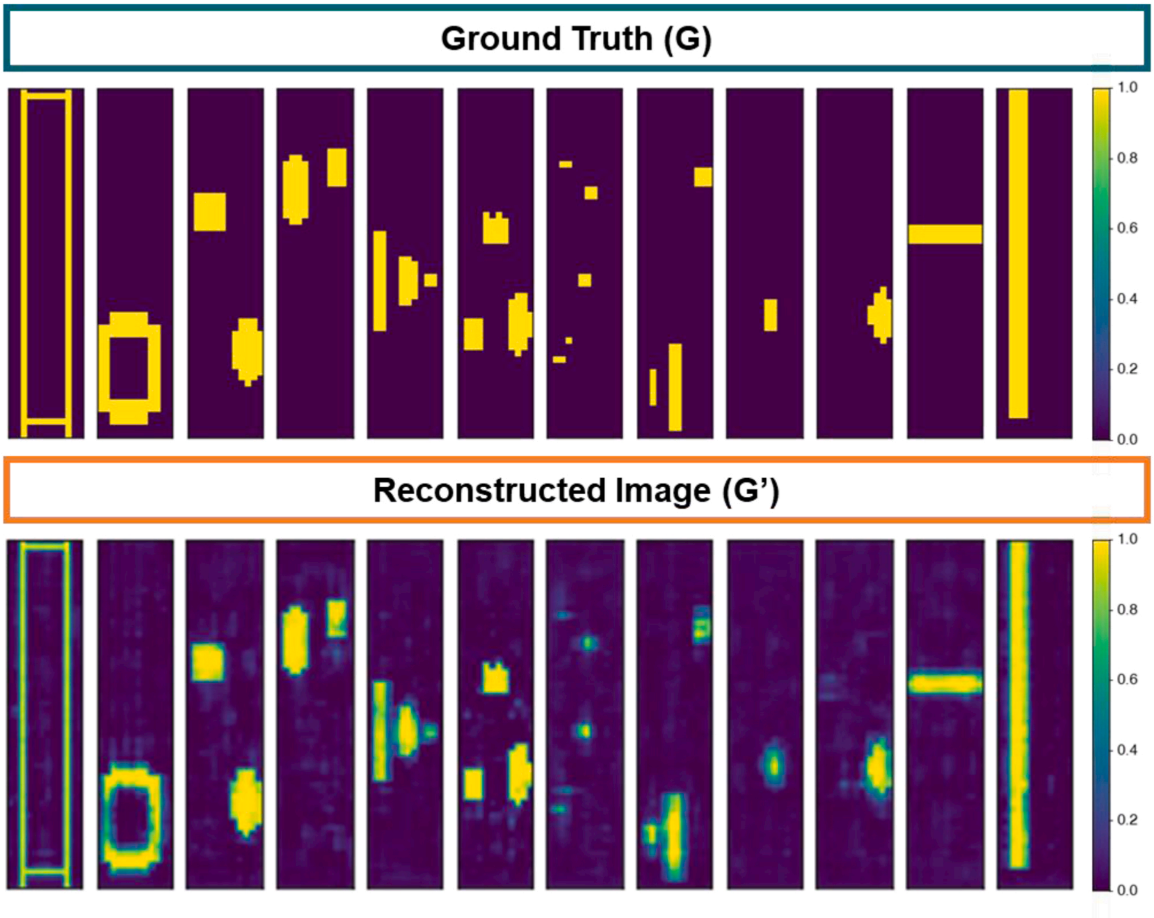

Fig. 8. The ground truth versus reconstructed image of the 12 unseen dataset samples showed excellent reconstruction capability of our proposed supervised autoencoder reconstruction algorithm.

$$cor(X, \widehat{X}) = \frac{\sum_{i=0}^{n-1} [x_i - E(X)][\widehat{x_i} - E(\widehat{X})]}{\sqrt{\sum_{i=0}^{n-1} [x_i - E(X)]^2 \sum_{i=0}^{n-1} [\widehat{x_i} - E(\widehat{X})]^2}} \tag{12}$$

where X and $\widehat{X}$ are two matrices with the same dimensions, x_i and $\widehat{x_i}$ are the i^{th} element and $E(X)$ and $E(\widehat{X})$ are the expected values of X and $\widehat{X}$ respectively.

3.2. Model evaluation and testing results

A simple single hidden layer supervised autoencoder is implemented in Python with Tensorflow to reconstruct the relative permittivity distribution within the seal area. The decoder of the autoencoder model is used to generate the reconstructed image for evaluation. The optimized model is trained with a batch size of 32, a learning rate of 0.0001, 8000 epochs, and the weights α_x and α_y are set as 0.45 and 0.85 respectively. The 10-fold cross-validation results are shown in Table 2. The average MSE and COR scores are 0.0319 and 0.6703 respectively. Corresponding to the results presented in Table 2, Fig. 7 shows the reconstruction quality of the particle distribution visually in each fold. In general, the autoencoder performs well to distributions with larger particles such as the round, through, and mix, but experiences significant reconstruction noise when the particles are smaller in the scatter and spot categories. The contrast between regions with and without particles reduces as the particles decrease in size and become isolated, as shown by the cloudy images in Fig. 7. To reduce the reconstruction noise, additional data samples with noise integration can be collected to further optimize the supervised autoencoder model. While some of the cross-validated images have a low COR score and high MSE, the visual effect of these image reconstructions is still very close to the actual permittivity distribution, which is sufficient to serve as a guide for online quality assurance.

The unseen test dataset contains two sample images from each category and both the actual and reconstructed relative permittivity distributions of the twelve samples are shown in Fig. 8. With a supervised autoencoder, the reconstructed image reflects the true relative permittivity distribution within the seal region accurately even in conformal sensor placement, which significantly improves the sensing resolution. The reconstructed relative permittivity distribution images have shown an accurate representation of materials within the seal both visually and quantitatively. Most importantly, the supervised approach learns the underlying physics process and captures the relevant relationship between the capacitance matrix and the real permittivity distribution, ensuring the strong relevance of the reconstruction model. Lastly, the reconstruction speed is extremely fast using only 1.1 ms on a regular workstation computer with an Intel Core i5 CPU for each relative permittivity distribution image. This is due to the facile autoencoder architecture used. We expect the performance of the reconstruction model to be enhanced with more complex neural network architecture and additional data. The model can then be seamlessly integrated into the production line for real-time defect detection, ensuring maximum production speed at minimum wastage and downtime. The same technique can also be extended to other types of sensor placement based on the application to satisfy the sensor resolution requirements.

4. Conclusion

In this paper, an electric field sensing system for package quality assurance is introduced. As the quality of defect detection depends heavily on both the sensor sensitivity and data representation, a conformal placement of electrodes coupled with a supervised autoencoder neural network reconstruction technique is proposed. Leveraging on the enhanced sensor sensitivity derived from the conformal placement of electrodes, the high-quality reconstructed relative permittivity distribution of the sensed region unveils valuable spatial information for defect detection. By using a simple network structure, the optimized autoencoder model achieved an average 10-fold cross-validation MSE and COR scores of 0.0319 and 0.6703, respectively. Furthermore, the reconstruction takes only 1.1 ms on commodity hardware and is ideal for real-time defect detection on the production line, ensuring maximum production speed with minimum wastage and downtime.

However, there are still several drawbacks that stand in the way of successful real-life implementation. Firstly, it is time-consuming and difficult to acquire a substantial well-labeled dataset for the development of an accurate reconstruction model. Secondly, the actual packages and contents vary significantly in shape, size, material, and sealing process that requires meticulous data preparation to ensure the quality of the developed model. Lastly, the measured electrical properties and the ground truth must be carefully defined and enforced throughout the data preparation stage. It is also crucial for the dataset to contain sufficient defect cases in different environments to improve the generalizability of the trained model. To overcome these limitations, we propose an automatic data collection and labeling system that provides an improved reference for calibration and evaluation. The proposed system acquires X-ray images with a commercial X-ray inspection machine, photo images with high-resolution cameras, and reconstructed capacitive images with our autoencoder-enabled capacitive sensor array. Firstly, the X-ray and camera images can be used directly as the reference for capacitive sensing calibration to ensure hardware quality and precision. Secondly, the X-ray, camera, and reconstructed images are cross-referenced and combined through physics-guided data fusion to capture more precise ground truth and establish dependable evaluation metrics. Finally, the newly introduced data not only improves the accuracy and robustness of the trained autoencoder model but also provides valuable feedback to enhance our simulation model. The improved simulation model can subsequently generate a more comprehensive dataset with a more elaborate distribution of defects on command to complement the limited experimental dataset.

Despite the above-mentioned limitations, the COMSOL simulation and generated dataset not only provide a strong physics-based verification of the feasibility of the system but also act as a guideline for experimental data preparation, thus bringing the aforementioned system a step closer to industrial implementation.

Funding sources

This work was supported by the National University of Singapore (NUS) Institute of Higher Learnings (IHLs) Technology Acceleration Program (TAP) (Grant Ref: R-263–000-D50–118), Singapore National Research Foundation’s Returning Singapore Scientist Scheme (Grant Ref: NRF-RSS2015–003), AME programmatic funding scheme of Cyber Physiochemical Interface (CPI) project (No. A18A1b0045), and the Singapore Hybrid-Integrated Next-Generation μ-Electronics (SHINE) Centre hosted at the National University of Singapore (NUS).

CRediT authorship contribution statement

Jieming Pan: Conceptualization, Methodology, Software, Formal analysis, Project administration, Writing. **Zaifeng Yang**: Software, Methodology, Review. **Stephanie Hui Kit Yap**: Formal analysis, Review. **Xiangyu Zhang**: Investigation, Formal analysis, Review. **Zefeng Xu**: Formal analysis, Validation, Review. **Yida Li**: Conceptualization, Resources, Review. **Yuxuan Luo**: Methodology, Resources, Review. **Evgeny Zamburg**: Resources, Project administration, Review. **En-Xiao Liu**: Software, Methodology, Review. **Chen-Khong Tham**: Methodology, Resources, Supervision, Review. **Aaron Voon-Yew Thean**: Methodology, Fund acquisition, Resources, Supervision, Review.

Conflicts of interest statement

The authors have declared no conflict of interest.

Acknowledgment

none.

Appendix A. Supporting information

Supplementary data associated with this article can be found in the online version at doi:10.1016/j.fpsl.2022.100919.

References

Alzubaidi, L., Zhang, J., Humaidi, A. J., Al-Dujaili, A., Duan, Y., Al-Shamma, O., … Farhan, L. (2021). Review of deep learning: Concepts, CNN architectures, challenges, applications, future directions. *Journal of Big Data, 8*(1), 53. https://doi.org/10.1186/s40537-021-00444-8

Andersen, A. H., & Kak, A. C. (1984). Simultaneous algebraic reconstruction technique (SART): A superior implementation of the ART algorithm. *Ultrasonic Imaging, 6*(1), 81–94.

Arridge, S. R. (1999). Optical tomography in medical imaging. *Inverse Problems, 15*(2), R41.

Ayhan, Z., Zhang, Q., Farahbakhsh, B., & Kneller, M. (2001). Inspection of seal integrity of food packages using ultrasound and pressure differential techniques. *Applied Engineering in Agriculture, 17*(2), 179.

Bach, P. B., Mirkin, J. N., Oliver, T. K., Azzoli, C. G., Berry, D. A., Brawley, O. W., … Jett, J. R. (2012). Benefits and harms of CT screening for lung cancer: A systematic review. *Jama, 307*(22), 2418–2429.

Buzug, T. M. (2011). Computed tomography. *Springer Handbook of Medical Technology* (pp. 311–342). Springer.

Calvetti, D., & Reichel, L. (2003). Tikhonov regularization of large linear problems. *BIT Numerical Mathematics, 43*(2), 263–283.

Charles, J. H. (2013). *Handbook of nondestructive evaluation, second edition* (2nd ed.). New York: McGraw-Hill Education.

De Schryver, T., Dhaene, J., Dierick, M., Boone, M. N., Janssens, E., Sijbers, J., … Van Hoorebeke, L. (2016). In-line NDT with X-ray CT combining sample rotation and translation. *NDT & E International, 84*, 89–98.

Dimitrov, K. C., Song, S., Chang, H., Lim, T., Lee, Y., & Kwak, B.-J. (2020). Interdigital capacitor-based passive LC resonant sensor for improved moisture sensing. *Sensors, 20*(21), 6306.

Gallagher, E., & Moussa, W. (2014). A study of the effect of the fringe fields on the electrostatic force in vertical comb drives. *Sensors (Basel, Switzerland), 14*(11), 20149–20164. https://doi.org/10.3390/s141120149

Golub, G. H., Hansen, P. C., & O’Leary, D. P. (1999). Tikhonov regularization and total least squares. *SIAM Journal on Matrix Analysis and Applications, 21*(1), 185–194.

Goodfellow, I., Pouget-Abadie, J., Mirza, M., Xu, B., Warde-Farley, D., Ozair, S., … Bengio, Y. (2014). Generative adversarial nets. *Advances in Neural Information Processing Systems, 27*.

Graves, M., Smith, A., & Batchelor, B. (1998). Approaches to foreign body detection in foods. *Trends in Food Science & Technology, 9*(1), 21–27. https://doi.org/10.1016/S0924-2244(97)00003-4

Gupta, M., Kumari, M., Jain, R., & Lakshay. (2021). super-resolution-based GAN for image processing: Recent advances and future trends. In A. Solanki, A. Nayyar, & M. Naved (Eds.), *Generative Adversarial Networks for Image-to-image Translation* (pp. 1–15). Academic Press.

Hamanaka, M.E., Segundo, A.K.R., & Silva, S.A.L. d. (2017, 29 Oct.–1 Nov. 2017). Portable non-invasive capacitive transducer for measuring fuel level. Paper presented at the 2017 IEEE SENSORS.

Hanke, M., Neubauer, A., & Scherzer, O. (1995). A convergence analysis of the landweber iteration for nonlinear ill-posed problems. *Numerische Mathematik, 72*(1), 21–37.

Herman, G. T. (2009). *Fundamentals of computerized tomography: Image reconstruction from projections*. Springer Science & Business Media.

Huang, G.-B., Zhu, Q.-Y., & Siew, C.-K. (2006). Extreme learning machine: Theory and applications. *Neurocomputing, 70*(1–3), 489–501.

Jia, X., Huang, J., Luan, H., Rozelle, S., & Swinnen, J. (2012). China’s milk scandal, government policy and production decisions of dairy farmers: The case of greater Beijing. *Food Policy, 37*(4), 390–400.

Kirsch, L. E. (2007). Package integrity testing. *Guide to Microbiological Control in Pharmaceuticals and Medical Devices*, 367–381.

Li, Y., Alian, A., Sivan, M., Huang, L., Ang, K. W., Lin, D., … Thean, A. V. Y. (2019). A flexible InGaAs nanomembrane PhotoFet with tunable responsivities in near- and short-wave IR region for lightweight imaging applications. *APL Materials, 7*(3), Article 031503. https://doi.org/10.1063/1.5074181

Li, Y., Luo, Y., Nayak, S., Liu, Z., Chichvarina, O., Zamburg, E., … Thean, A. V.-Y. (2019). A stretchable-hybrid low-power monolithic ECG patch with microfluidic liquid-metal interconnects and stretchable carbon-black nanocomposite electrodes for wearable heart monitoring. *Advanced Electronic Materials, 5*(2), 1800463. https://doi.org/10.1002/aelm.201800463

Li, Y., Nayak, S., Luo, Y., Liu, Y., Mohan, H., Pan, J., … Thean, A. V. Y. (2019). A soft polydimethylsiloxane liquid metal interdigitated capacitor sensor and its integration in a flexible hybrid system for on-body respiratory sensing. *Materials, 12*, 1458. https://doi.org/10.3390/ma12091458

Luiz, L. D. C., Bell, M. J. V., Batista, R. T., Freitas, R. P. D., Rocha, R. A. D., Moreira, S. I., … Anjos, V. D. C. D. (2021). Use of scanning electron microscopy with energy dispersive spectroscopy to detect metallic contamination in candies. *Food Packaging and Shelf Life, 28*, Article 100649. https://doi.org/10.1016/j.fpsl.2021.100649

Luo, Y., Li, Y., Thean, A.V., & Heng, C. (2020, 16–20 Feb. 2020). 23.2 A 70μW 1.19mm2 wireless sensor with 32 channels of resistive and capacitive sensors and edge-encoded PWM UWB transceiver. Paper presented at the 2020 IEEE International Solid-State Circuits Conference - (ISSCC).

Marashdeh, Q., Fan, L. S., Du, B., & Warsito, W. (2008). Electrical capacitance tomography – a perspective. *Industrial & Engineering Chemistry Research, 47*(10), 3708–3719. https://doi.org/10.1021/ie0713590

Morita, Y., Dobroiu, A., Otani, C., & Kawase, K. (2007). Real-time Terahertz diagnostics for detecting microleak defects in the seals of flexible plastic packaging. *Journal of Advanced Mechanical Design, Systems, and Manufacturing, 1*(3), 338–345. https://doi.org/10.1299/jamdsm.1.338

Pan, J., Li, Y., Luo, Y., Zhang, X., Wang, X., Wong, D. L. T., … Thean, A. V.-Y. (2021). Hybrid-flexible bimodal sensing wearable glove system for complex hand gesture recognition. *ACS Sensors*. https://doi.org/10.1021/acssensors.1c01698

Pan, J., Li, Y., Luo, Y., Zhang, X., Yang, Z., Wong, D.L.T., Niu, X., Tham, C.K., & Thean, A. V.Y. (2020, 25–28 Oct. 2020). Seal integrity testing utilizing non-destructive capacitive sensing for product packaging assurance. Paper presented at the 2020 IEEE SENSORS.

Pillai, K. P. P. (1970). Fringing field of finite parallel-plate capacitors. *Proceedings of the Institution of Electrical Engineers, 117*(6), 1201–1204. https://doi.org/10.1049/piee.1970.0232

Poiger, T., Kari, F. G., & Giger, W. (1999). Fate of fluorescent whitening agents in the river glatt. *Environmental Science & Technology, 33*(4), 533–539.

Raparia, D., Alessi, J., & Kponou, A. (1997). The algebraic reconstruction technique (ART). Paper presented at the Proceedings of the 1997 Particle Accelerator Conference (Cat. No. 97CH36167).

Raum, K., Ozguler, A., Morris, S. A., & O'Brien, W. D. (1998). Channel defect detection in food packages using integrated backscatter ultrasound imaging. *IEEE Transactions on Ultrasonics, Ferroelectrics, and Frequency Control, 45*(1), 30–40.

Reinas, I., Oliveira, J., Pereira, J., Mahajan, P., & Poças, F. (2016). A quantitative approach to assess the contribution of seals to the permeability of water vapour and oxygen in thermosealed packages. *Food Packaging and Shelf Life, 7*, 34–40. https://doi.org/10.1016/j.fpsl.2016.01.003

Sand, C. K. (2019). Testing the integrity of package seals. *Food Technology Magazine*, *73*.

Schoeman, L., Williams, P., du Plessis, A., & Manley, M. (2016). X-ray micro-computed tomography (μCT) for non-destructive characterisation of food microstructure. *Trends in Food Science & Technology, 47*, 10–24.

Shikhaliev, P. M. (2018). Large-scale MV CT for cargo imaging: A feasibility study. *Nuclear Instruments and Methods in Physics Research Section A: Accelerators, Spectrometers, Detectors and Associated Equipment, 904*, 35–43.

Smith, J., White, T., Dodge, C., Paradiso, J., Gershenfeld, N., & Allport, D. (1998). Electric field sensing for graphical interfaces. *IEEE Computer Graphics and Applications, 18*(3), 54–60. https://doi.org/10.1109/38.674972

Sun, B., Yue, S., Cui, Z., & Wang, H. (2015). A new linear back projection algorithm to electrical tomography based on measuring data decomposition. *Measurement Science and Technology, 26*(12), Article 125402.

Tiefenbacher, K. F. (2018). *The technology of wafers and waffles II: Recipes, product development and know-how*. Elsevier Science.

Van Loan, C. F. (1976). Generalizing the singular value decomposition. *SIAM Journal on Numerical Analysis, 13*(1), 76–83.

Wall, M. E., Rechtsteiner, A., & Rocha, L. M. (2003). Singular value decomposition and principal component analysis. *A Practical Approach to Microarray Data Analysis* (pp. 91–109). Springer.

Wang, L., Liu, X., Chen, D., Yang, H., & Wang, C. (2020). ECT image reconstruction algorithm based on multiscale dual-channel convolutional neural network. *Complexity, 2020*.

Whittaker, V. N. (1972). A review of non-destructive measurement of flaw size. *Non-Destructive Testing, 5*(2), 92–100. https://doi.org/10.1016/0029-1021(72)90101-6

WHO. 2022. Food safety. https://www.who.int/news-room/fact-sheets/detail/food-safety.

Wu, Y., Xian, Y., Guo, X., Chen, L., Zhao, X., Wang, B., & Wang, L. (2018). Development and validation of a screening and quantification method for simultaneous determination of seven fluorescent whitening agents in commercial flour using UPLC–MS/MS. *Food Chemistry, 243*, 162–167. https://doi.org/10.1016/j.foodchem.2017.09.110

Xiong, B., Li, Y., Thean, A., & Heng, C. (2019). A 7×7×2mm^3 8.60μ 500-kb/s transmitter with robust injection-locking based frequency-to-amplitude conversion receiver targeting for implantable applications. 2019 IEEE Custom Integrated Circuits Conference (CICC), 1–4.

Xu, L., Weber, A. P., & Kasper, G. (2000). Capacitance-based concentration measurement for gas-particle system with low particles loading. *Flowing Measurement and Instrumentation, 11*(3), 185–194. https://doi.org/10.1016/S0955-5986(00)00018-2

Yang, W., Lu, M., & Zhou, Y. (2018). Simulation study of sensor of ECT system based on comsol.

Yang, W., & Peng, L. (2002). Image reconstruction algorithms for electrical capacitance tomography. *Measurement Science and Technology, 14*(1), R1.

Yao, J., & Takei, M. (2017). Application of process tomography to multiphase flow measurement in industrial and biomedical fields: A review. *IEEE Sensors Journal, 17*(24), 8196–8205.

Yap, S. H. K., Pan, J., Linh, D. V., Zhang, X., Wang, X., Teo, W. Z., … Thean, A. V.-Y. (2022). Engineered nucleotide chemicapacitive microsensor array augmented with physics-guided machine learning for high-throughput screening of cannabidiol. *Small*, 2107659. https://doi.org/10.1002/smll.202107659

Ye, Y., Zhang, C., He, C., Wang, X., Huang, J., & Deng, J. (2020). A review on applications of capacitive displacement sensing for capacitive proximity sensor. *IEEE Access, 8*, 45325–45342. https://doi.org/10.1109/ACCESS.2020.2977716

Zhang, H., Zeng, L., Teng, H., & Zhang, X. (2017). A novel on-chip impedance sensor for the detection of particle contamination in hydraulic oil. *Micromachines, 8*(8), 249. https://doi.org/10.3390/mi8080249

Zheng, J., & Peng, L. (2018). An autoencoder-based image reconstruction for electrical capacitance tomography. *IEEE Sensors Journal, 18*(13), 5464–5474.

Zuo, Y., Wu, Y., Gu, J., & Zhang, Y. (2017). The UV aging properties of maleic anhydride esterified starch/polylactic acid composites. In *Journal of Wuhan University of Technology-Mater. Sci, 32* pp. 971–977).